

## Momentum-resolved electronic structure of LaTiO<sub>2</sub>N photocatalysts by resonant Soft-X-ray ARPES

Craig Lawley<sup>1,2</sup>, Arian Arab<sup>3</sup>, Anna Hartl<sup>1,2,3</sup>, Aleksandar Staykov<sup>4</sup>, Max Döbeli<sup>5</sup>, Thorsten Schmitt<sup>3</sup>, Daniele Pergolesi<sup>1</sup>, Thomas Lippert<sup>1,2,4</sup>✉ & Vladimir N. Strocov<sup>3</sup>✉

Oxynitrides are promising materials for visible light-driven water splitting. However, limited information regarding their electron-momentum resolved electronic structure exists. Here, with the advantage of the enhanced probing depth and chemical state specificity of soft-X-ray ARPES, we determine the electronic structure of the photocatalyst oxynitride LaTiO<sub>2</sub>N and monitor its evolution as a consequence of the oxygen evolution reaction. After the photoelectrochemical reactions, we observe a partial loss of Ti- and La-N 2p states, distortions surrounding the local environment of titanium atoms and, unexpectedly, an indication of an electron accumulation layer at or near the surface, which may be connected with either a large density of metallic surface states or downward band bending. The distortions and defects associated with the titanium 3d states lead to the trapping of electrons and charge recombination, which is a major limitation for the oxynitride LaTiO<sub>2</sub>N. The presence of an accumulation layer and its evolution suggests complex mechanisms of the photoelectrochemical reaction, especially in cases where co-catalysts or passivation layers are used.

<sup>1</sup>Laboratory for multiscale materials experiments, Paul Scherrer Institute, Forschungsstrasse 111, Villigen PSI 5232, Switzerland. <sup>2</sup>Department of Chemistry and Applied Biosciences, ETH Zürich, Zürich 8093, Switzerland. <sup>3</sup>Laboratory for condensed matter, Paul Scherrer Institute, Forschungsstrasse 111, Villigen PSI 5232, Switzerland. <sup>4</sup>International Institute for Carbon-Neutral Energy Research (I2CNER), Kyushu University, 744 Motooka, Fukuoka 819-0395, Japan. <sup>5</sup>Laboratory for Ion Beam Physics, ETH Zürich, Zürich 8093, Switzerland. ✉email: [thomas.lippert@psi.ch](mailto:thomas.lippert@psi.ch); [vladimir.strocov@psi.ch](mailto:vladimir.strocov@psi.ch)

In several oxide materials, the substitution of nitrogen into the oxygen site leads to the formation of the corresponding oxynitride material<sup>1</sup>. This substitution results in a significant reduction of the band gap, typically shifting the band gap from the ultra-violet region towards the visible light energy range<sup>2,3</sup>. Moreover, the edge positions of the valence band maximum (VBM) and conduction band minimum (CBM) for these oxynitrides are ideal for overall water splitting, as they incorporate both the water reduction and oxidation potentials<sup>4</sup>. With a band gap lying in the visible-light energy range and suitably aligned band positions, the perovskite oxynitride LaTiO<sub>2</sub>N (LTON) is a promising photocatalyst for visible-light solar water splitting<sup>5-7</sup>.

However, the surface of LTON initially evolves during operation conditions, limiting its long-term performance<sup>8</sup>. The design and discovery of new materials able to sustain an efficient solar water splitting process would represent an enormous breakthrough for the storage of solar energy in the form of a clean and renewable fuel<sup>9,10</sup>. To drive this advancement, it requires the discovery of novel or the improvement of existing materials, able to fulfill all the requirements to allow efficient solar-to-hydrogen conversion. Addressing this requires comprehensive understanding of the photocatalysts electronic structure and its evolution over the photoelectrochemical (PEC) reaction (PECR).

The most direct experimental method to probe the electronic structure is angle-resolved photoemission spectroscopy (ARPES), where one measures the distribution of photoelectrons as a function of their kinetic energy  $E_k$  and, emission angle  $\theta$  under irradiation of the sample by monochromatic photons with energy  $h\nu$ <sup>11</sup>. The electron-momentum ( $\mathbf{k}$ )-integrated electronic structure of oxynitrides has already been studied with X-ray photoelectron spectroscopy<sup>12-14</sup>. However, no  $\mathbf{k}$ -resolved information from ARPES experiments, pivotal in understanding details of the electronic structure of these materials, is available up to now. This can be explained by the fact that the standard ARPES in the vacuum ultra-violet (VUV) energy range has a probing depth of less than 0.5 nm<sup>15</sup>, which makes this technique extremely sensitive to surface contamination, unavoidably piling up during the ex-situ transfer of the as-grown sample to the ARPES experiment and destroying the chemical authenticity and crystallinity of the probed region.

In this work, we overcome this difficulty and directly access  $\mathbf{k}$ -resolved electronic structure of LTON by using soft-X-ray ARPES (SX-ARPES) in an energy range of several hundreds of eV, where the probing depth increases to a few nm beyond the surface contamination layer. Moreover, the SX-ARPES energy range covers the  $L$ -edges of the transition metals and  $M$ -edges of rare-earth elements, which are characteristic components of oxynitrides (Ti and La in LTON's case, respectively). This will allow us to use resonant photoexcitation at the Ti  $L$ - and La  $M$ -edges (resonant SX-ARPES) to complement the  $\mathbf{k}$ -resolution of the ARPES experiment, by elemental and even chemical-state resolution<sup>16-18</sup>. First, we will establish the  $\mathbf{k}$ - and chemical-state-resolved electronic structure of LTON and, second, follow its evolution associated with photocatalytic reaction.

## Results and Discussion

**Experimental strategy.** Figure 1a shows the geometry and schematic representation of a typical ARPES experiment. Here, monochromatic X-rays from a synchrotron source are incident on the oxynitride thin film under ultra-high vacuum (UHV) conditions. Due to the photoelectric effect, photoelectrons are emitted from the sample. A hemispherical electron energy analyser detects the escaped photoelectrons as a function of their kinetic energies ( $E_k$ ) and emission angles (polar  $\theta$  and azimuthal  $\phi$ ) depending on the incoming photon energy,  $h\nu$ . In this case, the

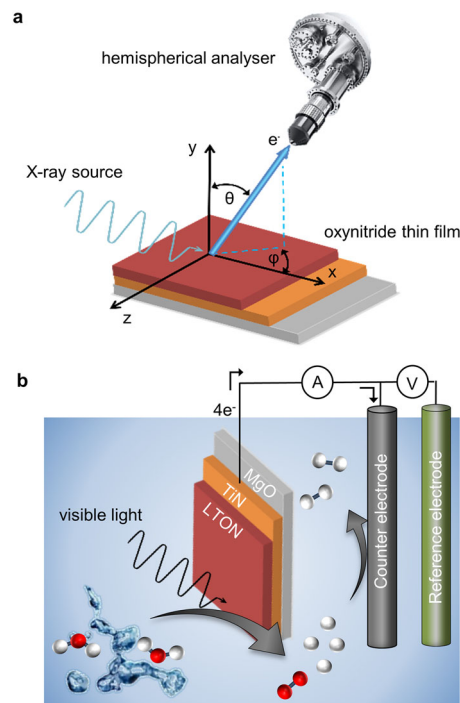


**Fig. 1 Experimental overview.** **a** Schematic of an ARPES experiment showing the photoemission geometry. **b** three-electrode configuration for the PEC characterisation. The red and white spheres represent oxygen and hydrogen, respectively.

energy conservation yields the binding energy of these electrons ( $E_B$  relative to the Fermi level  $E_F$ ) back in the sample as:

$$E_b = E_k - h\nu + \phi \quad (1)$$

where  $\phi$  is the work function. Equally important for the photoemission process, involving direct transitions, is the experimental information on the electron momentum  $\mathbf{k}$  of the valence states. In the ARPES experiment on crystalline systems, the surface-parallel momentum ( $\mathbf{k}_{xy}$ ) is conserved and can be found as:

$$\mathbf{k}_{xy} = \frac{\sqrt{2m}}{\hbar} \sqrt{E_k} \sin \theta + p_{xy} \quad (2)$$

where  $p_{xy}$  is the photon-momentum correction.

In this work, we utilize resonant SX-ARPES to measure a number of LTON oxynitride photocatalyst thin films in their as-grown states and after the PECR. Our results elucidate the electronic structure of the LTON oxynitride thin film surface layers and, its associated evolution during the oxygen evolution reaction.

The photocatalytic conversion of solar energy into a clean, low cost, renewable fuel source can be realised by the splitting of water into molecular H<sub>2</sub> and O<sub>2</sub>. However, the water splitting reaction is an energetically unfavourable reaction, requiring a standard Gibbs free energy change of +237.2 kJ mol<sup>-1</sup> (1.23 eV per electron). Therefore, to produce H<sub>2</sub> and O<sub>2</sub> from water requires a light absorbing semiconductor (SC) photocatalyst to assist in the process. This material must possess a band gap larger than the theoretical minimum (1.23 eV), to account for kinetic overpotentials and, the band positions must be sufficiently positioned to account for the redox potentials for the hydrogen evolution and oxygen evolution reactions (HER and OER, respectively)<sup>19</sup>.

The oxynitride LTON, satisfies these criteria with a band gap of ca. 2.1 eV<sup>20</sup>. The band gap is large enough to absorb photons with energy  $\geq 1.23$  eV but is also responsive to visible light wavelengths (ca. 590 nm) unlike many of the wide-band gap oxide materials,

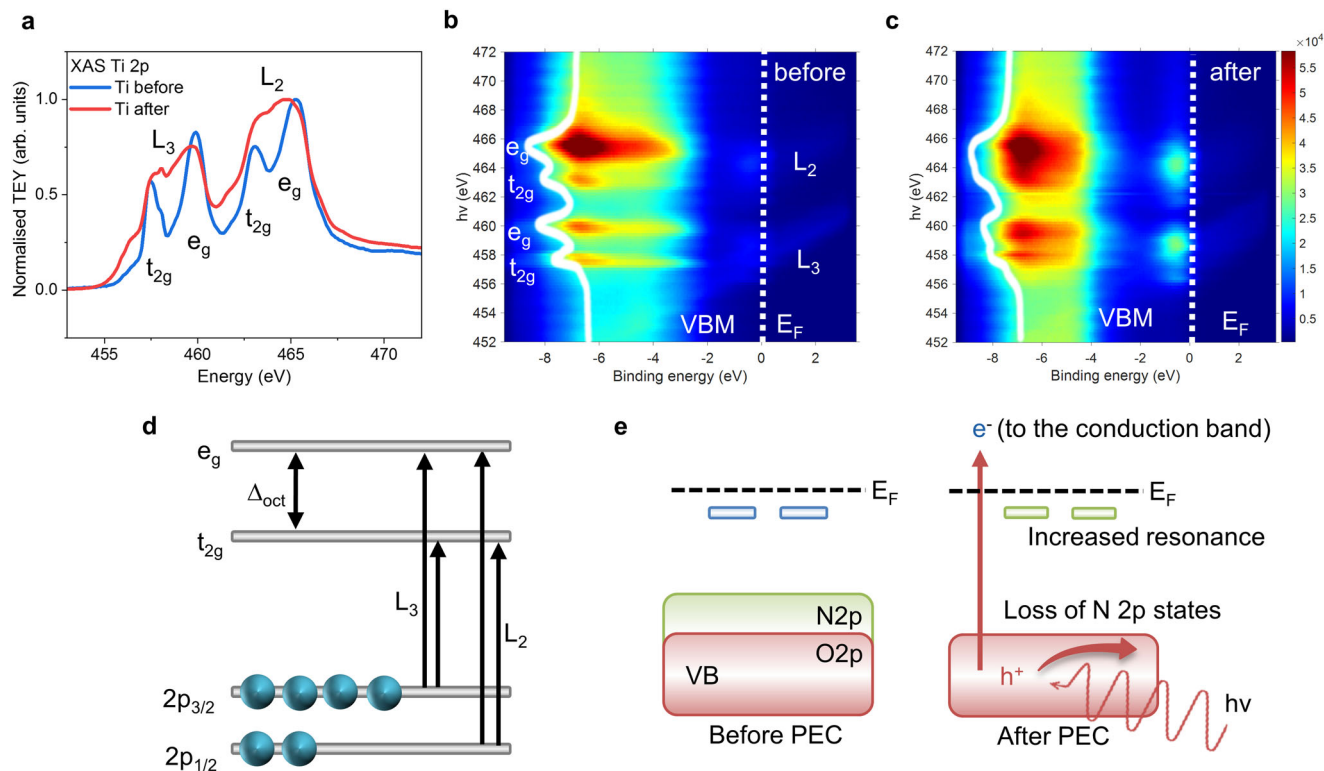


**Fig. 2 Titanium B cation resonant SX-ARPES.** **a** XAS spectra for LTON showing the Ti  $L_2$  and  $L_3$  edge before and after the PECR, shown in blue and red, respectively. **b, c** Maps of angle-integrated ResPE intensity across the Ti  $L_3$  and  $L_2$  before (**b**) and after (**c**) the PECR. The solid white lines are the XAS spectra overlaid from (**a**). The white dashed line marks the  $E_F$  (0 eV). **d** Schematic representation of the transition of the  $L_3$  and  $L_2$  absorption bands. **e** Graphic representation for the observed changes occurring to the band structure of the surface layers of the LTON photocatalyst, where  $h\nu$  and VB denote the visible-light photons and the VB, respectively.

which are responsive only to the UV part of the solar spectrum. As schematised in Fig. 1b, upon light irradiation (photons) with energy greater than or equal to that of the band gap the photon is absorbed, creating electron-hole pairs. Excited from the valence band (VB) to the conduction band (CB), the electrons then travel via the TiN electrical contact buffer layer to the Pt counter electrode, where the electrons can directly reduce protons to form  $H_2$ . The photogenerated holes left behind in the valence band migrate to the surface of LTON where, they are then consumed in the oxidation of water, generating  $O_2$ . The reference electrode sets the 0V potential and an increasing voltage bias is applied between the working and counter electrode. The electronic current (photocurrent) between the working and counter electrodes is then proportional to the amount of  $H_2$  and  $O_2$  produced.

In the following sections, we employ resonant SX-ARPES, complemented by soft-X-ray absorption spectroscopy (XAS), to study the evolution of the  $k$ - and elemental-character resolved electronic structure of the oxynitride before and after the PECR. The LTON thin film morphologies and PEC characterisation are included in Supplementary Fig. 1, 2, respectively.

**Resonant SX-ARPES: Titanium B cation.** First, we will follow the electronic structure of the Ti ions in the B site of the perovskite LTON ( $ABO_2N$ ). Figure 2 shows the soft-X-ray XAS spectra measured at the Ti  $L_2$  (460.2 eV) and  $L_3$  (453.8 eV) edges. The  $L_2$  and  $L_3$  electronic transitions correspond to the photo-excitation from the Ti  $2p_{1/2}$  and Ti  $2p_{3/2}$  states to the unoccupied Ti  $3d$  states, respectively (Fig. 2d). The Ti  $3d$  peaks before the PECR (blue) are split by the crystal-field ( $\Delta_{oct}$ ) into the  $t_{2g}$  and  $e_g$  states. After the PECR (red) the main peaks of  $L_2$  and  $L_3$  edges do

not exhibit any change in position (energy), which suggest no change in oxidation state for Ti. However, the peak splitting is no longer resolved, suggesting a lattice distortion surrounding the absorbing Ti cation and a lowering of symmetry of the octahedra, likely due to vacancy generation. This has previously been shown for LTON measured at the Ti  $K$  edge using hard X-ray grazing-incidence X-ray absorption spectroscopy (GIXAS)<sup>8</sup>. However, the  $K$  edge spectra are sensitive to the  $3d$  and  $4p$  orbitals. In our case, XAS at the  $L$ -edges involve electric dipole allowed  $2p$  to  $3d$  transitions and therefore, neglecting the multiplet effects<sup>21</sup>, reflect the Ti  $d$  states. Vacancy generation should result in  $Ti^{3+}$  states, which may contribute to the small pre-resonance intensity. However, due to a combination of the crystal-field splitting, distortions to the octahedral environment, and multiplet effects, elucidation of various contributions would require reference materials<sup>22</sup> to be measured extensively and compared experimentally and theoretically<sup>23</sup>.

The experimental maps of (angle-integrated) resonant photo-emission (ResPE) intensity as a function of  $E_B$  and  $h\nu$  are shown in Fig. 2 parts b and c, before and after the PECR, respectively. In the first approximation, neglecting the multiplet effects in the ResPE process<sup>16,17,21,24</sup>, the resonating intensity represents the admixture of Ti weight to the VB states, with those near the bottom and top of the VB being derived from the O  $2p$  and N  $2p$  states, respectively, hybridised with the Ti states. The resonant intensity appears on top of a large non-resonant spectral contribution (in Fig. 2b, the intensity at ca. 452–454 eV).

The XAS spectra (Fig. 2a) are overlaid to the ResPE maps in Fig. 2 parts b and c as the solid white line, where the four XAS peaks correspond to the hotspots of the resonating intensity. After the PECR (Fig. 2c), we observe considerably widened XAS peaks and the resonating-intensity hotspots in excitation energy.

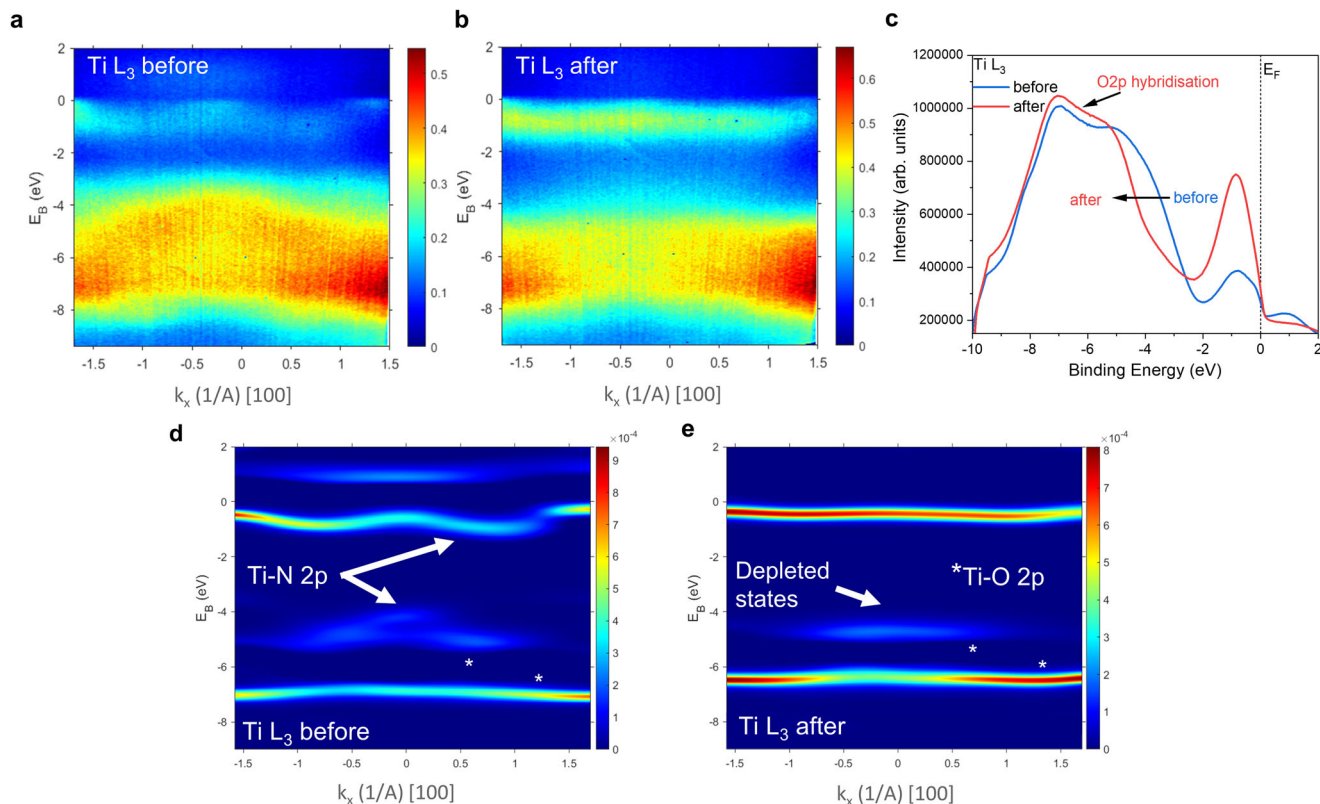


**Fig. 3** Titanium B cation high-statistics ARPES data. **a, b**  $Ti L_3$ -edge high-statistics ARPES images acquired at  $h\nu = 465.3$  eV before (**a**) and after (**b**) the PECR. **c** Angle-integrated ARPES images from **a, b**, **d, e** the ARPES data from **a, b** represented in the second derivative  $-d^2/dE_B^2$  to enhance the band dispersions. The parallel  $Ti L_2$ -edge data are included in Supplementary Fig. 4.

Moreover, after the PECR there is an increase in the  $L_3$  resonating intensity of the  $Ti - O 2p$  states at the bottom of the VB. This may suggest creation of additional  $Ti - O 2p$  states and increased hybridisation between their respective valence orbitals. This observation would be in agreement with previous reports for perovskite oxynitrides with vacancy healing by O species under OER conditions<sup>20</sup> and perovskite oxides, which exhibit increases in hydrophilicity and undergo surface reconstructions during the OER, resulting in a superficial enriched B cation - OH/O(OH) surface layer and an increase in catalytic activity<sup>25–27</sup>.

As previously described, upon the O to N substitution in LTON, N  $2p$  states are introduced that lie higher in energy than the O  $2p$  states, shifting the VB maximum (VBM) upwards and reducing the band gap (Fig. 2e). In the as grown sample (before the PECR), the VBM, which consists of  $Ti - N 2p$  states, is situated below the  $E_F$  at ca.  $-3$  to  $-4$  eV. After the PECR (Fig. 2c), the N  $2p$  derived states partially deplete, which results in the loss of intensity at the VBM between  $-3$  and  $-4$  eV. Furthermore, the resonating intensity near the  $E_F$  (just below 0 eV) dramatically increases after the PECR, indicating that new defect states emerge in this energy region. Consistently with the loss of the N  $2p$  states near the VBM, we conjecture that these states are split off the Ti-derived states constituting the CBM of LTON. It has been suggested that LTON has a direct bandgap<sup>28</sup>, which is in line with previous reports for  $LaTiO_xN_y$ <sup>6</sup>. However, as this is usually inferred via UV-vis spectroscopy<sup>29,30</sup>, there are also reports for LTON through theoretical calculations suggesting it has both direct and indirect points<sup>31</sup>. As it is not possible to observe the unoccupied states using ARPES, we are unable to experimentally determine whether LTON possesses a direct or indirect bandgap. That said, the emerging states split of the CBM suggest that we observe an indirect band gap for LTON.

The reduced intensity of the VBM suggests that bulk N leaves the lattice structure. It remains however, interstitial/chemisorbed on the surface in the form of  $N_2$  and  $NO_x$  species as corroborated by XPS data<sup>7,32</sup>. As the surface-lattice N and the OER intermediates (OH/O(OH)) likely react in competitive side reactions<sup>27,33–35</sup>, it is possible that the increase in hydrophilicity and a superficial B cation-OH/O(OH) enriched surface layer, normally associated with the perovskite oxides, will have a more antagonistic role with respect to the oxynitrides.

We now complement the  $k$ -integrated ResPE maps in Fig. 2 by high-statistics  $k$ -resolved measurements at the  $Ti L_2$  and  $L_3$  edges, providing direct information on the band dispersions and their evolution across the PECR (Fig. 3).

Parts a-b, presents the ARPES intensity images at the  $L_3$  edge (the results at the  $L_2$  edge are similar and are presented in Supplementary Fig. 4) before and after the PECR, respectively, and  $k_x$  describes the component of  $k$  parallel to the surface of LTON along the Miller Indices,  $hkl$  [100]. The resonance emphasises the O and N  $2p$  states hybridised with the Ti states. To discriminate the band dispersions, the angle-integrated spectral intensity is subtracted in these ARPES images from the raw intensity. Furthermore, the parts d-e emphasize the spectral peaks using the negative second derivative  $-d^2/dE_B^2$  of the (Gaussian pre-smoothed) spectral intensity (with the  $-d^2/dE_B^2 < 0$  values, having no direct physical meaning, set to zero). The data processing steps can be seen in Supplementary Fig. 3.

We observe dispersive VB states near the VBM and at ca.  $-4$  eV. The very fact of  $k$ -dependent electron energies attests good crystallinity of our samples. The partial loss of the N  $2p$  states near the VBM after the PECR is associated with flattening of the electron dispersion in this energy region. We also note that the states near the  $E_F$  (just below 0 eV), which we have previously



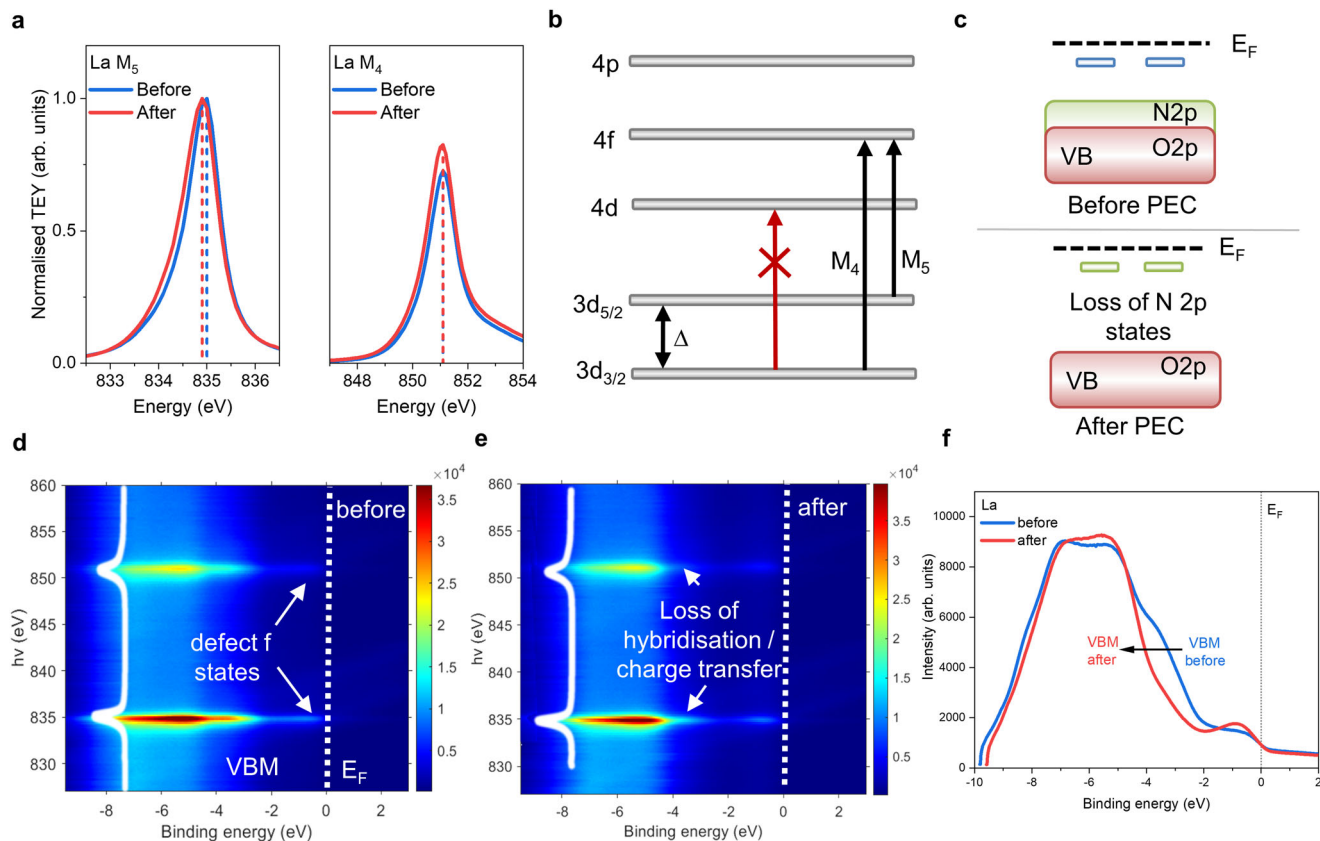


**Fig. 4 Lanthanum A cation resonant SX-ARPES.** **a** XAS spectra for LTON showing the La  $M_5$  and  $M_4$  edges, respectively. **b** Schematic representation of the transitions of the  $M_4$  and  $M_5$  absorption bands. **c** Schematic representation of the La contribution to the band structure of LTON. **d** La resonance (angle-integrated) PE intensity map before PECR. **e** After PECR. **f** Angle-integrated plots for data shown in parts **d**, **e**.

assigned to the Ti-derived states split off from the CBM, scale up in intensity after the PECR but also flatten their dispersion. The loss of dispersion and reduction of the band curvature suggests reduced orbital overlap and, in turn, a weaker hybridization which could be associated with the formation of an accumulation layer. The high-statistics Ti  $L_2$  measurements (Supplementary Fig. 4) show the same effect but with reduced resonating intensity, due to the relative strengths of the  $L_2$  and  $L_3$  transitions.

**Resonant SX-ARPES: Lanthanum A cation.** We will now follow the electronic structure of La ions in the A site of LTON. Figure 4a shows the XAS spectra for LTON measured at the La  $M_5$  (836 eV) and  $M_4$  (853 eV) edges. These involve the electronic transitions of the La  $3d_{5/2}$  and  $3d_{3/2}$  states to the unoccupied La  $4f$  states, respectively (Fig. 4b). Due to selection rules<sup>36</sup> the  $3d > 4d$  transition is forbidden, as shown by the red arrow. The transition to the  $4p$  state is allowed, however, this process has much smaller cross-section compared to the  $4f$  resonance and is shifted into higher photon energies. The two main peaks in the  $3d > 4f$  XAS spectrum of LTON arise due to spin-orbit coupling, with the spin-orbit splitting between the peaks being ca. 16.2 eV, in line with previous reports<sup>37,38</sup>. After the PECR, the splitting of these peaks increases slightly due to a reductive shift of the  $M_5$  peak in  $E_B$  of ca. 0.1–0.15 eV (Fig. 4a), accompanied by an increase in its energy width, with the amplitude unchanged. The  $M_4$  peak also increases its width after the PECR, but its energy does not shift and has a notable increase of its amplitude. These changes can be explained by the partial covalence between the La  $5d$  and O  $2p$  states upon the formation of  $\text{LaO}_x/\text{LaOH}$  at the surface. Here, La behaves as a transition metal, albeit a poor one. It retains partial

$d$ -electron ( $5d^1$ ) density<sup>8,39–43</sup>, used in hybridisation and the partial covalence between the O  $2p$  states.

The maps of (angle-integrated) ResPE intensity at the  $M$ -edge of La are included in Fig. 4d–f. The resonant intensity enhancement for La is weaker compared to the Ti resonance (Figs. 3c, 4f) which is expected since the sites of O and N, forming the VB, are situated on the octahedral sites of the Ti cation. Interestingly though, we can see resonating spectral intensity just below the  $E_F$  (just below 0 eV) as also observed for the Ti resonance.

This fact suggests that La  $4f$  states hybridise with the N  $2p$  ones forming the VBM at ca.  $-3$  to  $-4$  eV, yet the majority of the La resonant weight is contributed by the La – O  $2p$  hybridised states lower in the VB. We note, however, that in the case of La the multiplet effects in ResPE<sup>21</sup> are much more pronounced than for Ti, and the relation of the ResPE intensity to the La weight in the VB states becomes less direct.

**Experimental vs theoretical Density of States (DOS).** The experimental  $k$ -integrated DOS is qualitatively represented by off-resonant angle-integrated ARPES spectra, albeit modulated by photoemission matrix elements depending on  $E_B$  the binding and  $h\nu$  excitation energies. Figure 5, parts a and b presents such spectra measured just below the Ti  $L_3$  and La  $M_5$  resonances, respectively. The gross features of both spectra are the VB extending over the  $E_B$  range from  $-9$  to  $-3$  eV, and a narrow band just below the  $E_F$  (0 eV). The spectral modulations in the VB region are however, different because of the matrix elements<sup>44</sup> depending on  $h\nu$ . The experimental angle-integrated spectra can be considered representative of the DOS (notwithstanding the fact that the PE intensity is modulated by the matrix elements and

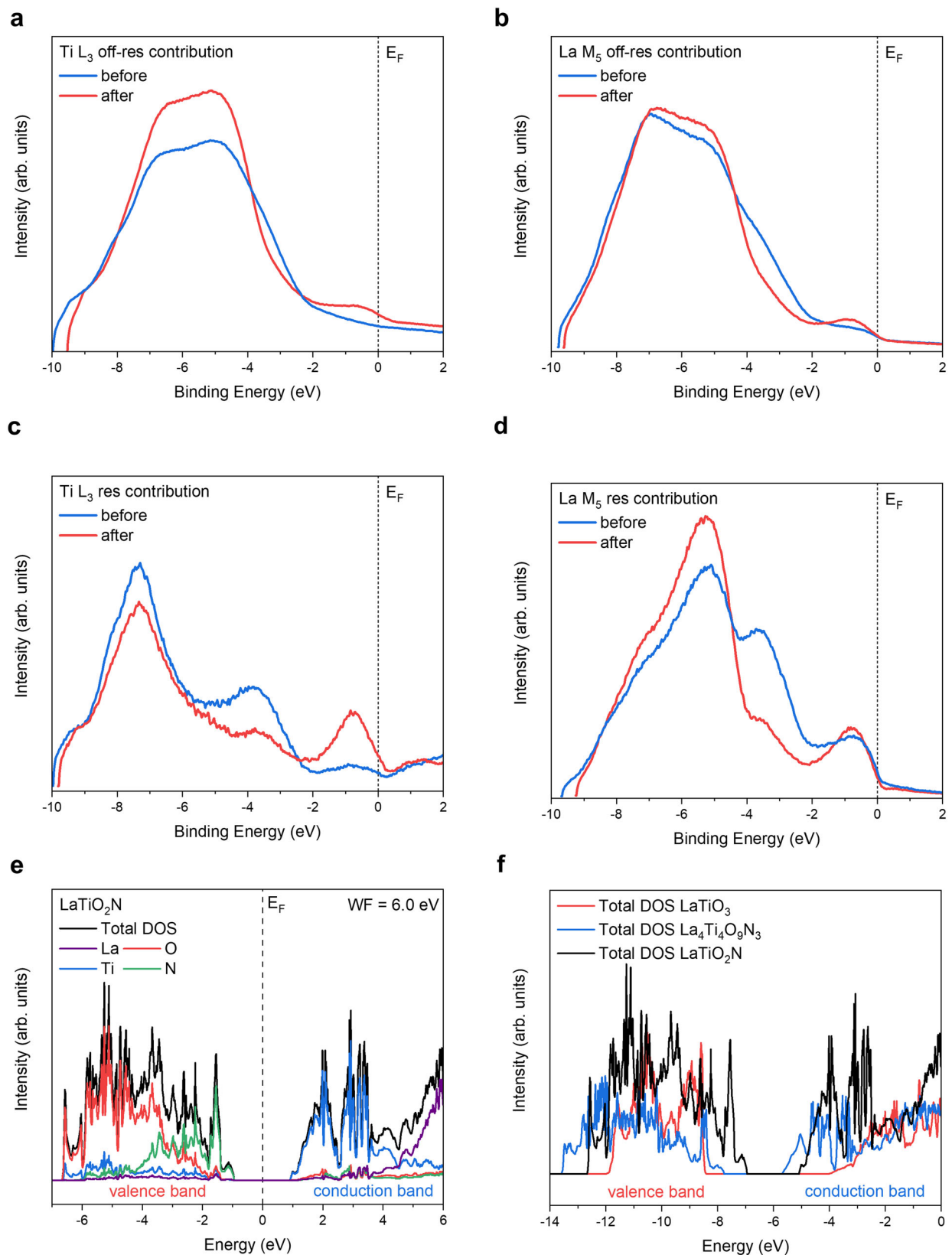


**Fig. 5 Experimental vs. theoretical DOS.** **a** Off-resonant angle-integrated ARPES spectra measured below the Ti L<sub>3</sub> edge (averaged over  $h\nu = 452\text{--}454$  eV) representing the total DOS. **b** The La M<sub>5</sub> edge ( $h\nu = 828\text{--}830$  eV). **c** Resonant weight (resonant minus off-resonant spectral intensity) at the Ti L<sub>3</sub> edge ( $h\nu = 460.2$  eV). **d** The La M<sub>5</sub> edge ( $h\nu = 835$  eV) representing the Ti and La partial DOS, respectively. The spectra (**a–d**) are measured before and after the PECR. **e** Total and partial DOS for LaTiO<sub>2</sub>N. **f** Total DOS for LaTiO<sub>2</sub>N, LaTiO<sub>3</sub> and La<sub>4</sub>Ti<sub>4</sub>O<sub>9</sub>N<sub>3</sub>, aligned to the Fermi level.

the angular integration extends over a limited angular range falling into the acceptance of the ARPES analyzer).

The element-resolved partial DOS (PDOS) can qualitatively be determined from the ResPE angle-integrated spectra where, neglecting the multiplet effects<sup>21</sup>, the resonant intensity difference relative to the off-resonant spectra represents the weight of the resonating element in the electron states<sup>16,17,24</sup>. Such differential spectra for the Ti  $L_3$  and La  $M_5$  edges, representing the Ti and La partial DOS, respectively, are shown in Fig. 5c, d. To help our understanding of LTON's electronic structure and afterwards its evolution over the PECR, we will compare the experimental data with Density-Functional Theory (DFT) calculations (see Experimental Section) for stoichiometric LaTiO<sub>2</sub>N.

Figure 5e shows, the calculated total and the PDOS for Ti, O, N and La, aligned to  $E_F$ , with the work function calculated as 6.0 eV. The band gap of LaTiO<sub>2</sub>N is 1.9 eV, which is close to the experimentally reported values<sup>1,45</sup>. The calculations confirm the commonly accepted picture of LTON's electronic structure where the states near the VB bottom are formed mostly by O  $2p$  atomic orbitals and near the VBM mostly by the N  $2p$  orbitals. With the reservation for the matrix elements, the calculated total DOS is in a reasonable agreement with the experimental VB in Fig. 5a, b. Turning to the Ti PDOS hybridized mostly with the O  $2p$  states, the calculations suggest its notable increase towards the VB bottom. This is confirmed by the experimental Ti PDOS derived from the ResPE data, Fig. 5c, that indeed scales up in this energy region. The calculated partial La PDOS is weighted towards the VB centre, which is also consistent with the ResPE results in Fig. 5d.

There are however significant deviations of the experiment from the calculations: (1) the experimental VB ( $-3$  eV) in Fig. 5a is deeper in  $E_B$  by  $\sim 1.5$  eV, and (2) there is a narrow band just below the  $E_F$  (0 eV) which, according to the Ti ResPE data in Fig. 2b, c and the derived Ti PDOS in Fig. 5c, has a large Ti weight. These observations can be reconciled with the theory if the  $E_F$  shifts upwards into the Ti derived CB. This means, however, that the surface layer of our LTON sample, probed in our ARPES experiment, should be metallic. We conjecture that, with the intrinsically semiconducting bulk of LTON, the presence of such a metallic surface layer may be explained by either a large density of surface states or downward band bending towards the surface.

**Electronic structure evolution across the PECR.** Consistently with the previous works<sup>7,46–48</sup>, our DFT calculations confirmed by the experimental ResPE data have shown that the VBM ( $-3$  to  $-4$  eV) below the  $E_F$  (0 eV) is comprised of the Ti and La states hybridised with the N  $2p$  ones, whereas in the bottom of the VB these states hybridise with the O  $2p$  ones. The angle-integrated ARPES intensity for the above high-statistics measurements at the Ti  $L_3$  edge are included in Fig. 3c. Here, it is easier to follow the evolution of the DOS in LTON and the changes with respect to the OER. Confirming our observations in the ResPE maps in Fig. 2b, c, we observe an increase in the total resonating intensity after the PECR, which suggests creation of additional O  $2p$  states or a greater degree of hybridisation in the bottom of the VB (ca.  $-5$  to  $-8$  eV).

We also observe reduced intensity of the VBM ( $-3$  to  $-4$  eV) due to the partial loss of lattice N at/near the surface of LTON under OER conditions. Effectively, this would mean a lower probability of photon absorption in the visible light region due to loss of states near the VBM.

The same two effects can also be observed in the La ResPE map and the angle-integrated plot, shown in Fig. 4 parts e and f, respectively.

In Fig. 5, we compare the Ti (c) and La (d) resonant contributions, representing the weight of the Ti and La hybridised states in the VB of LTON, before and after the PECR. After the PECR, we can see a slight loss of the La and Ti weight at the VBM ( $-3$  eV). We attribute this evolution of the spectra to the partial loss of lattice N at the surface during the OER, whereby the La-N and Ti-N hybridized states near the VBM ( $-3$  eV) partially deplete.

For comparison with the evolution of LTON after the PECR, in Fig. 5f we compare the calculated total DOS for the stoichiometric LTON with that for the unstable LaTiO<sub>3</sub> (LTO) and the anion-deficient defect structure La<sub>4</sub>Ti<sub>4</sub>O<sub>9</sub>N<sub>3</sub> (D-LTON). For the sake of clarity, only the spin-up contributions have been included in this comparison (the total DOS for LTO and D-LTON are included in the Supplementary Fig. 6). These materials were chosen with their respective elemental compositions to reflect possible trends to the electronic structure of LTON upon the loss of N and creation of anion vacancies and/or changing the O/N content, as suggested by the resonant SX-ARPES data evolution over the PECR. To compare the three materials more accurately, the energy scale of their DOS was aligned to the  $E_F$  level (0 eV). We note that the DOS of LTO and D-LTON show that the  $E_F$  (0 eV) of these materials lies in the CB, which is composed of anti-bonding states. Their occupation is unfavourable, because it would destabilise the lattice, resulting in its reorganisation. Usually, such reorganisations proceed via phase transformations or due to vacancy formation, which explains why LTO does not exist as a natural mineral. Furthermore, we note that both LTO and D-LTON are spin polarised since Ti has the formal charge  $3^+$  in LTO, whereas D-LTON is a non-stoichiometric material (the spin-up/spin-down decomposition of their DOS is given in Supplementary Fig. 6).

Comparing the total DOS in Fig. 5f, we can see that the partial or total loss of N in the anion-deficient D-LTON or in the unstable LTO shifts the VBM downwards in energy (ca. 2 and 4.5 eV, respectively). This further suggests that during the OER, the O/OH<sup>-</sup> intermediates are involved in the photocatalytic formation of nitrate and nitrite species from the surface lattice N atoms<sup>27,33,35</sup> whereby they leave the lattice and remain chemisorbed on the surface in the form of NO<sub>x</sub> species<sup>7</sup>. This effect is consistent with the observed suppression of electron dispersions in the CB near the  $E_F$ . Furthermore, we conjecture diffusion of O atoms to heal remnant oxygen vacancies into LTON, generated upon loss of N from the lattice structure, from the O\* and OH<sup>-</sup> reactionary intermediates generated during the OER<sup>49</sup>. This is consistent with a slight increase of the VB intensity (at ca.  $-4$  to  $-7$  eV) in the off-resonant spectra, Fig. 5a, b, after the PECR.

However, the resonant weighted contributions for Ti and La (Fig. 5c, d) show that the La resonating intensity in the bottom of the VB increases, suggesting increased La – O  $2p$  hybridization, whereas that for Ti decreases. This can be explained by the fact that many such oxides and oxynitride SCs exhibit a preferential AO surface termination (LaO in the case of LTON) as experimentally determined by low energy ion spectroscopy (LEIS)<sup>26,50–52</sup>. The B cation, usually a transition metal cation, conventionally acting as the active site for oxygen evolution, would be hidden below the first atomic surface layer. Therefore, surface oxygen/nitrogen vacancies, would expose the underlying transition metal cations.

Previous calculations for LaTiO<sub>2</sub>N<sup>53</sup> have also suggested that the more oxygen added to the La-O surface layer, the more the SC is self-doped with electrons (accumulation) filling the empty Ti  $3d$  states. We see certain evidence of this effect in the La resonant spectrum (Fig. 5d) which shows increased O hybridisation, whereas, the Ti resonant spectrum (Fig. 5c) shows an increase of



the Ti 3*d* weight just below the  $E_F$  (0 eV) after the PECR. It was also suggested in the same work<sup>53</sup> that the evolution of the surface results in a geometrical configuration where two N atoms leave the Ti layer and move to the La surface layer, resulting in a more stable 5-coordinated Ti configurations.

Previous work<sup>8</sup> suggests that LTON undergoes a surface reconstruction with Ti showing signs of vacancy generation (resulting in an under-coordinated Ti) with the charge surrounding Ti, conserved. Usually, such reorganisations proceed via phase transformations or vacancy formation. In line with our observations, LTON could also generate O<sub>2</sub> under OER conditions by the proposed lattice oxygen evolution reaction (LOER) mechanism, as reported for oxide perovskite catalysts<sup>54–56</sup>. This would result in a surface layer that becomes more metallic, which may be connected with either a large density of metallic surface states or downward band bending.

The downward band bending would be contrary to our expectations, due to the fact that LTON is an n-type SC material where upward band bending would typically be assumed<sup>57,58</sup>. However, this contradiction has been experimentally observed for ZnO, which exhibits downward band bending at the ZnO/air interface after generation of vacancies by preferential O sputtering by ion bombardment in vacuum<sup>59</sup>. This would mean for the photoanode LTON, instead of the typically assumed formation of a depletion layer and upward band bending, LTON forms an electron-accumulation layer. This would also suggest that LTON would be better suited as a photocatalyst for the HER, the other half of the overall water-splitting reaction. Coming with this conjecture is a plethora of further questions: what occurs to the electronic structure of LTON when employed as a photocathode instead of a photoanode? what is the electronic structure at the semiconductor-co-catalyst interface? how does it evolve? what are the mechanisms during the PECR? The answers should take into account, not only the enhanced performance previously reported for oxynitrides<sup>8,60,61</sup> but also, the new findings in this work.

## Conclusion

In this work, we have determined the electronic structure of the oxynitride LTON photocatalyst resolved in *k*- and elemental character of the electronic states, and monitored its evolution through the PECR. Whereas no such information regarding oxynitrides existed to date, crucial to achieve it in the present study have been the *k*-resolution, enhanced probing depth and elemental/chemical-state specificity of synchrotron-radiation based resonant SX-ARPES. By combing the SX-ARPES results with the DFT calculations, we have established that the bottom of the VB consists of La and Ti states hybridised with the O 2*p* states, whereas the top of the VB consists of both La- and Ti - N 2*p* states.

Not only have we determined the electronic structure of the LTON photocatalyst, but also monitored its evolution caused by the OER. After the PECR, we observe (a) partial loss of Ti- and La-N 2*p* states, (b) distortion in the local environment of Ti, likely due to O/N vacancy generation, (c) the creation of additional La - O 2*p* states in the VB, and (d) the suggested formation of an electron accumulation layer in the surface region, suggesting either a large density of metallic surface states or downward band bending towards the surface. Along with the distortion and defects associated with Ti 3*d* states, the latter would lead to the trapping of electrons and charge recombination. Therefore, resonant SX-ARPES has been able to confirm this effect as one of the major limitations for the oxynitride LTON's functionality.

Passivation layers and co-catalysts have shown to increase the long-term performance of oxynitrides<sup>61</sup> by reducing charge

recombination as one of the benefits. However, the presence of the accumulation layer and its evolution across the PECR suggested by our results implies involvement of more complex mechanisms. The extension of our work to these buried interfaces, taking into advantage the probing depth and chemical specificity of resonant SX-ARPES, will allow us to rationalise/correlate the evolution of their electronic structure with respect to the increase in catalytic performance usually observed with the powder photocatalysts<sup>60,62</sup>. The spectroscopic abilities of resonant SX-ARPES highlighted by our work extend from the oxynitrides to a wide range of other thin-film and interface systems used in various functional materials.

## Methods

**Thin film deposition.** The thin films used in this work were grown using a modified pulsed laser deposition (PLD) method known as Reactive Crossed-beam Laser Ablation (PRCLA)<sup>63</sup>. A laser fluence of ca. 2.5 J cm<sup>-2</sup> was used at a repetition rate of 10 Hz. Commercially available MgO(001) substrates (10.0 × 0.5 × 0.5 mm) were used as a template to grow the TiN buffer layer and LTON thin film with a substrate-to-target distance fixed at 50 mm. Pt black paste was used for thermal contact between the substrate and heating stage. The substrate temperature was set to 750 °C, monitored via the emissivity using a pyrometer during the deposition. For TiN, a base pressure of 10<sup>-6</sup> mbar was used. For the deposition of the LTON films, the oxide target La<sub>2</sub>Ti<sub>2</sub>O<sub>7</sub> was ablated in the presence of a N<sub>2</sub> background with a pressure of 10<sup>-4</sup> mbar and NH<sub>3</sub> pulsed gas jets synchronized to the laser.

**Angle-resolved photoemission spectroscopy.** The ARPES measurements were performed at the SX-ARPES endstation<sup>64</sup> of the Advanced Resonant Spectroscopies (ADDRESS) beamline<sup>65</sup> situated at the Swiss Light Source, Paul Scherrer Institute, Switzerland. Resonant photoexcitations were performed at the Ti L<sub>2</sub>, L<sub>3</sub> and La M<sub>4</sub>, M<sub>5</sub> edges ( $E_0 = 460, 453, 853$  and 836 eV, respectively). The photon flux was ca. 10<sup>13</sup> photons/s and focused into a spot size of 30 × 75 μm<sup>2</sup> on the sample surface at an x-ray grazing incidence angle of 20°. The energy resolution was set to 140 meV and the sample temperature was kept at 20 K in order to maximise the coherent spectral component<sup>47</sup>. The angle-integrated spectra were integrated within ± 8°. The XAS data were measured in total electron yield (TEY).

We also performed time dependence measurements upon X-ray irradiation, to observe if the electronic structure of LTON is modified due to exposure to the X-ray beam. Only insignificant changes have been observed (Supplementary Fig. 5), which were comparable with the noise of the measurements and could be explained by X-ray stimulated desorption of surface contaminations. It is also possible that these changes were a consequence of the oxidation of hydrocarbons chemisorbed on the surface during the ex-situ transfer of the samples.

**Density functional theory.** Geometry optimisations and energy calculations were performed using DFT and Perdew-Burke-Ernzerhof (PBE)<sup>66</sup> functional implemented in the QuantumWise software package (now part of Synopsis)<sup>67</sup>. A pseudopotential method was applied using numerical atomic orbitals for representation of the valence electrons. The electron correlation was taken into account using the DFT-1/2 computational approach which allows for accurate estimation of band gaps in complex oxide materials<sup>68</sup>. Workfunctions were calculated for slabs with BO<sub>2</sub> termination<sup>69</sup> using ghost atom approach and multigrid Poisson solver with Neumann boundary condition (bottom surface) and Dirichlet boundary condition (top surface). The method allows to estimate the workfunctions of polar slabs which are not accessible without complicated surface reconstruction using planewave wavefunctions. Eight BO<sub>2</sub> layers were considered in each slab. Real space grid and *k*-point mesh have been converged to 10<sup>-4</sup> eV energies.

**Photoelectrochemical characterisation.** The PEC measurements were performed using a three-electrode configuration. A KCl saturated Ag/AgCl electrode was used as the reference. The oxynitride thin film and platinum wire were utilised as the working and counter electrode, respectively. An aqueous solution of 0.5 molar NaOH was used as an electrolyte with a pH of 13. The samples were illuminated with a 150 W Xe arc lamp (Newport 66477) with an AM 1.5 G filter with an output intensity of 100 mW cm<sup>-2</sup>. To measure the dark and light current a chopper was used to intermittently block the irradiation of the sample. The potentiodynamic and potentiostatic measurements were performed at a scan rate of 10 mV s<sup>-1</sup>.

**Composition analysis.** Rutherford Backscattering (RBS) and Elastic Recoil Detection Analysis (ERDA) were employed to determine the chemical compositions of the LTON thin films. RBS provides the metal ratios and oxygen content, whereas ERDA provides the nitrogen-to-oxygen ratio. The RBS measurements were conducted using a 2 MeV He beam and a silicon PIN diode detector. ERDA utilised a 13 MeV <sup>127</sup>I beam in combination with a time-of-flight spectrometer and a gas ionisation detector. RBS data was analysed using RUMP<sup>70</sup>.



**Crystalline properties.** XRD measurements were performed using a Seifert X-ray Diffractometer with characteristic Cu  $K_{\alpha}$  radiation,  $\lambda = 0.154$  nm.  $\theta$ - $2\theta$  scans were performed to determine the out-of-plane orientations of the films found in Supplementary Fig. 1.

## Data availability

The data portrayed in this work is available from the corresponding author upon reasonable request.

Received: 25 August 2021; Accepted: 7 February 2023;

Published online: 20 February 2023

## References

- Xie, R.-J., Bert Hintzen, H. T. & Johnson, D. Optical properties of (Oxy) Nitride materials: A review. *J. Am. Ceram. Soc.* **96**, 665–687 (2013).
- Pichler, M. et al. Determination of conduction and valence band electronic structure of LaTiOxNy thin film. *Chem. Sus. Chem.* **10**, 2099–2106 (2017).
- Moriya, Y., Takata, T. & Domen, K. Recent progress in the development of (oxy)nitride photocatalysts for water splitting under visible-light irradiation. *Coord. Chem. Rev.* **257**, 1957–1969 (2013).
- Takata, T. & Domen, K. Development of non-oxide semiconductors as light harvesting materials in photocatalytic and photoelectrochemical water splitting. *Dalton Trans.* **46**, 10529–10544 (2017).
- Minegishi, T., Nishimura, N., Kubota, J. & Domen, K. Photoelectrochemical properties of LaTiO<sub>2</sub>N electrodes prepared by particle transfer for sunlight-driven water splitting. *Chem. Sci.* **4**, 1120–1124 (2013).
- Le Paven-Thivet, C. et al. Photoelectrochemical properties of crystalline perovskite Lanthanum titanium oxynitride films under visible light. *J. Phys. Chem. C* **113**, 6156–6162 (2009).
- Pichler, M. et al. LaTiOxNy Thin Film Model Systems for Photocatalytic Water Splitting: Physicochemical Evolution of the Solid-Liquid Interface and the Role of the Crystallographic Orientation. *Adv. Funct. Mater.* **27**, 1605690 (2017).
- Lawley, C. et al. Examining the surface evolution of LaTiOxNy an oxynitride solar water splitting photocatalyst. *Nat. Commun.* **11**, 1178 (2020).
- Maeda, K. & Domen, K. Photocatalytic Water Splitting: Recent Progress and Future Challenges. *J. Phys. Chem. Lett.* **1**, 2655–2661 (2010).
- Hisatomi, T. & Domen, K. Reaction systems for solar hydrogen production via water splitting with particulate semiconductor photocatalysts. *Nat. Catalysis* **2**, 387–399 (2019).
- Damascelli, A., Hussain, Z. & Shen, Z. X. Angle-resolved photoemission studies of the cuprate superconductors. *Rev. Mod. Phys.* **75**, 473–541 (2003).
- Cristea, D. et al. Tantalum Oxynitride thin films: Assessment of the photocatalytic efficiency and antimicrobial capacity. *Nanomaterials (Basel)* **9** (2019).
- Seo, J. et al. The effects of annealing barium niobium oxynitride in argon on photoelectrochemical water oxidation activity. *J. Mater. Chem. A* **7**, 493–502 (2019).
- Hsu, J.-C., Lin, Y.-H. & Wang, P. W. X-ray Photoelectron spectroscopy analysis of nitrogen-doped TiO<sub>2</sub> films prepared by reactive-ion-beam sputtering with various NH<sub>3</sub>/O<sub>2</sub> gas mixture ratios. *Coatings* **10**, 47 (2020).
- Powell, C. J., Jablonski, A., Tilinin, I. S., Tanuma, S. & Penn, D. R. Surface sensitivity of Auger-electron spectroscopy and X-ray photoelectron spectroscopy. *J. Electron. Spectrosc. Relat. Phenom.* **98**, 1–15 (1999).
- Molodtsov, S. L. et al. Angle-resolved resonant photoemission as a probe of spatial localization and character of electron states. *Phys. Rev. Lett.* **78**, 142–145 (1997).
- Kobayashi, M. et al. Unveiling the impurity band induced ferromagnetism in the magnetic semiconductor (Ga,Mn)As. *PhRvB* **89**, 205204 (2014).
- Chikina, A. et al. Orbital Ordering of the Mobile and Localized Electrons at Oxygen-Deficient LaAlO<sub>3</sub>/SrTiO<sub>3</sub> Interfaces. *ACS Nano*. **12**, 7927–7935 (2018).
- Chen, S. & Wang, L.-W. Thermodynamic Oxidation and reduction potentials of photocatalytic semiconductors in aqueous solution. *Chem. Mater.* **24**, 3659–3666 (2012).
- Maegli, A. E. et al. Perovskite-Type LaTiO<sub>2</sub>N Oxynitrides for solar water splitting: Influence of the synthesis conditions. *Energy Procedia* **22**, 61–66 (2012).
- de Groot, F. Multiplet effects in X-ray spectroscopy. *Coord. Chem. Rev.* **249**, 31–63 (2005).
- Degroot, F. M. F. et al. 2p X-Ray Absorption of Titanium in Minerals. *Phys. Chem. Miner.* **19**, 140–147 (1992).
- Krüger, P. Multichannel multiple scattering calculation of L<sub>2,3</sub>-edge spectra of TiO<sub>2</sub> and SrTiO<sub>3</sub>: Importance of multiplet coupling and band structure. *PhRvB*. **81**, 125121 (2010).
- Olson, C. G. et al. Valence-band dispersion in angle-resolved resonant photoemission from LaSb. *Phys. Rev. Lett.* **76**, 4265–4268 (1996).
- Sun, X., Wu, F., Liu, G. & Xu, X. Enabling efficient visible light photocatalytic water splitting over SrTaO<sub>2</sub>N by incorporating Sr in its B site. *J. Mater. Chem. A* **6**, 20760–20768 (2018).
- Chen, Y. et al. Segregated Chemistry and Structure on (001) and (100) Surfaces of (La<sub>1-x</sub>Sr<sub>x</sub>)<sub>2</sub>CoO<sub>4</sub> Override the crystal anisotropy in oxygen exchange kinetics. *Chem. Mater.* **27**, 5436–5450 (2015).
- Kato, H. & Kudo, A. Photocatalytic reduction of nitrate ions over tantalate photocatalysts. *Phys. Chem. Chem. Phys.* **4**, 2833–2838 (2002).
- Yuan, L.-D., Deng, H.-X., Li, S.-S., Wei, S.-H. & Luo, J.-W. Unified theory of direct or indirect band-gap nature of conventional semiconductors. *PhRvB* **98**, 245203 (2018).
- Makula, P., Pacia, M. & Macyk, W. How To Correctly Determine the Band Gap Energy of Modified Semiconductor Photocatalysts Based on UV-Vis Spectra. *J. Phys. Chem. Lett.* **9**, 6814–6817 (2018).
- Cooper, J. K. et al. Indirect Bandgap and Optical Properties of Monoclinic Bismuth Vanadate. *J. Phys. Chem. C* **119**, 2969–2974 (2015).
- Castelli, I. E., Pandey, M., Thygesen, K. S. & Jacobsen, K. W. Band-gap engineering of functional perovskites through quantum confinement and tunneling. *PhRvB* **91**, 165309 (2015).
- Lawley, C. et al. Protagonists and spectators during photocatalytic solar water splitting with SrTaOxNy oxynitride. *J. Mater. Chem. A* **10**, 2374–2387 (2022).
- Yuan, S. J. et al. Nitrate formation from atmospheric nitrogen and oxygen photocatalysed by nano-sized titanium dioxide. *Nat. Commun.* **4**, 2249 (2013).
- Wei, L., Adamson, M. A. S. & Vela, J. Ni<sub>2</sub>P-Modified Ta<sub>3</sub>N<sub>5</sub> and TaON for Photocatalytic Nitrate Reduction. *Chemnanomat* **6**, 1179–1185 (2020).
- Dai, C., Sun, Y., Chen, G., Fisher, A. C. & Xu, Z. J. Electrochemical Oxidation of Nitrogen towards Direct Nitrate Production on Spinel Oxides. *Angew. Chem. Int. Ed. Engl.* **59**, 9418–9422 (2020).
- Tanner, P. A. & Duan, C.-K. Luminescent lanthanide complexes: Selection rules and design. *Coord. Chem. Rev.* **254**, 3026–3029 (2010).
- Kaya, Ç. et al. Influence of Gallium Substitution on the Crystal and Electronic Properties of Li<sub>5</sub>Ca<sub>1-x</sub>Ga<sub>x</sub>La<sub>3</sub>Zr<sub>2</sub>O<sub>12</sub> Solid State Battery Electrolyte. *J. Electron Spectrosc. Relat. Phenom.* **226**, 45–52 (2018).
- Lagarde, P., Flank, A. M., Ogasawara, H. & Kotani, A. Resonant photoemission of La and Yb at the 3d absorption edge. *J. Electron Spectrosc. Relat. Phenom.* **128**, 193–204 (2003).
- Loble, M. W. et al. Covalency in lanthanides. An X-ray absorption spectroscopy and density functional theory study of LnCl<sub>6</sub>(x-) (x = 3, 2). *J. Am. Chem. Soc.* **137**, 2506–2523 (2015).
- Wu, J. et al. A systematic evaluation of the role of lanthanide elements in functional complex oxides; implications for energy conversion devices. *J. Mater. Chem. A* **6**, 11819–11829 (2018).
- Ritzmann, A. M., Dieterich, J. M. & Carter, E. A. Density functional theory + U analysis of the electronic structure and defect chemistry of LSCF (La<sub>0.5</sub>Sr<sub>0.5</sub>Co<sub>0.25</sub>Fe<sub>0.75</sub>O<sub>3-δ</sub>). *Phys. Chem. Chem. Phys.* **18**, 12260–12269 (2016).
- Lee, Y.-L. & Morgan, D. Ab initio defect energetics of perovskite (001) surfaces for solid oxide fuel cells: A comparative study of LaMnO<sub>3</sub> versus SrTiO<sub>3</sub> and LaAlO<sub>3</sub>. *PhRvB* **91** (2015).
- Akbay, T. et al. The interaction of molecular oxygen on LaO terminated surfaces of La<sub>2</sub>NiO<sub>4</sub>. *Journal of Materials Chemistry A* **4**, 13113–13124 (2016).
- Lindroos, M., Sahrakorpi, S. & Bansil, A. Matrix element effects in angle-resolved photoemission from Bi<sub>2</sub>Sr<sub>2</sub>CaCu<sub>2</sub>O<sub>8</sub>: Energy and polarization dependencies, final state spectrum, spectral signatures of specific transitions, and related issues. *PhRvB* **65**, 054514 (2002).
- Haydous, F. et al. Oxynitride Thin Films versus Particle-Based Photoanodes: A Comparative Study for Photoelectrochemical Solar Water Splitting. *ACS Appl. Energy Mater.* **2**, 754–763 (2019).
- Ninova, S. & Aschauer, U. Anion-order driven polar interfaces at LaTiO<sub>2</sub>N surfaces. *J. Mater. Chem. A* **7**, 2129–2134 (2019).
- Yashima, M. et al. Imma perovskite-type oxynitride LaTiO<sub>2</sub>N: structure and electron density. *Chem. Commun. (Camb)* **46**, 4704–4706 (2010).
- Shi, J. et al. LaTiO<sub>2</sub>N-LaCrO<sub>3</sub>: continuous solid solutions towards enhanced photocatalytic H<sub>2</sub> evolution under visible-light irradiation. *Dalton Trans.* **46**, 10685–10693 (2017).
- Ouhbi, H. & Aschauer, U. Nitrogen Loss and Oxygen Evolution Reaction Activity of Perovskite Oxynitrides. *ACS Mater. Lett.* **1**, 52–57 (2019).
- Druce, J. et al. Surface termination and subsurface restructuring of perovskite-based solid oxide electrode materials. *Energy Environ. Sci.* **7**, 3593–3599 (2014).
- Staykov, A. et al. Oxygen Activation and Dissociation on Transition Metal Free Perovskite Surfaces. *Chem. Mater.* **27**, 8273–8281 (2015).

52. Rupp, G. M. et al. Surface chemistry of La<sub>0.6</sub>Sr<sub>0.4</sub>CoO<sub>3-δ</sub> thin films and its impact on the oxygen surface exchange resistance. *J. Mater. Chem. A* **3**, 22759–22769 (2015).
53. Ninova, S. & Aschauer, U. Surface structure and anion order of the oxynitride LaTiO<sub>2</sub>N. *J. Mater. Chem. A* **5**, 11040–11046 (2017).
54. Liu, J. et al. Dynamic Lattice Oxygen Participation on Perovskite LaNiO<sub>3</sub> during Oxygen Evolution Reaction. *J. Phys. Chem. C* **124**, 15386–15390 (2020).
55. Pan, Y. et al. Direct evidence of boosted oxygen evolution over perovskite by enhanced lattice oxygen participation. *Nat. Commun.* **11**, 2002 (2020).
56. Schweinar, K., Gault, B., Mouton, I. & Kasian, O. Lattice Oxygen Exchange in Rutile IrO<sub>2</sub> during the Oxygen Evolution Reaction. *J. Phys. Chem. Lett.* **11**, 5008–5014 (2020).
57. Singh, R. B. et al. Trapped state sensitive kinetics in LaTiO<sub>2</sub>N solid photocatalyst with and without cocatalyst loading. *J. Am. Chem. Soc.* **136**, 17324–17331 (2014).
58. Zhang, Z. & Yates, J. T. Jr. Band bending in semiconductors: chemical and physical consequences at surfaces and interfaces. *Chem. Rev.* **112**, 5520–5551 (2012).
59. Tosi E., Comedi D. & Zampieri G. Band bending at the ZnO(0001)-Zn surface produced by electropositive, electronegative and atmospheric adsorbates. *Appl. Surf. Sci.* **495**, 143592 (2019).
60. Yamakata, A. et al. Behavior and Energy States of Photogenerated Charge Carriers on Pt- or CoOx-Loaded LaTiO<sub>2</sub>N Photocatalysts: Time-resolved visible to mid-infrared absorption study. *J. Phys. Chem. C* **118**, 23897–23906 (2014).
61. Haydous, F. et al. Improved Photoelectrochemical Water Splitting of CaNbO<sub>2</sub>N Photoanodes by CoPi Photodeposition and Surface Passivation. *J. Phys. Chem. C* **123**, 1059–1068 (2018).
62. Maeda, K. Photocatalytic water splitting using semiconductor particles: History and recent developments. *J. Photochem. Photobiol. C: Photochem. Rev.* **12**, 237–268 (2011).
63. Willmott, P. R. Pulsed reactive crossed-beam laser ablation. *Appl. Phys. a-Mater. Sci. Processing* **69**, S437–S440 (1999).
64. Strocov, V. N. et al. Soft-X-ray ARPES at the Swiss light source: From 3D materials to buried interfaces and impurities. *Synchrotron Radiat. News* **27**, 31–40 (2014).
65. Strocov, V. N. et al. Soft-X-ray ARPES facility at the ADDRESS beamline of the SLS: concepts, technical realisation and scientific applications. *J. Synchrotron Radiat.* **21**, 32–44 (2014).
66. Hammer, B., Hansen, L. B. & Nørskov, J. K. Improved adsorption energetics within density-functional theory using revised Perdew-Burke-Ernzerhof functionals. *PhRvB* **59**, 7413–7421 (1999).
67. Smidstrup, S. et al. QuantumATK: An integrated platform of electronic and atomic-scale modelling tools. *J. Phys. Condens. Matter.* **32**, 015901 (2020).
68. Doumont, J., Tran, F. & Blaha, P. Limitations of the DFT-1/2 method for covalent semiconductors and transition-metal oxides. *PhRvB* **99**, 115101 (2019).
69. Jacobs, R., Booske, J. & Morgan, D. Understanding and controlling the work function of perovskite oxides using density functional theory. *Adv. Funct. Mater.* **26**, 5471–5482 (2016).
70. Doolittle, L. R. A Semiautomatic algorithm for rutherford backscattering analysis. *Nuclear Instrum. Meth. Phys. Res. Sec. B-Beam Interactions Mater. Atoms* **15**, 227–231 (1986).

## Acknowledgements

The authors would like to thank the Paul Scherrer Institute and ETH Zurich for financial support. A. A. acknowledges the support from the Swiss National Science Foundation within the grant 200020B\_188709.

## Author contributions

Conceptualisation—C.L., A.A., T.L., and V.S.; Investigation—C.L., A.A., A.S., M.D., and V.S.; Formal Analysis—C.L., A.A., A.S., V.S., A.H., and M.D.; Writing-Original Draft—C.L., A.H., and V.S.; Writing-Review & Editing—C.L., A.H., A.A., T.S., A.S., D.P., T.L., M.D., and V.S.; Funding Acquisition—V.S., T.S., and T.L.; Supervision—V.S., D.P., and T.L.

## Competing interests

The authors declare no competing interests.

## Additional information

**Supplementary information** The online version contains supplementary material available at <https://doi.org/10.1038/s43246-023-00344-9>.

**Correspondence** and requests for materials should be addressed to Thomas Lippert or Vladimir N. Strocov.

**Peer review information** *Communications Materials* thanks Kenichi Ozawa and the other, anonymous, reviewer(s) for their contribution to the peer review of this work. Primary Handling Editor: Aldo Isidori.

**Reprints and permission information** is available at <http://www.nature.com/reprints>

**Publisher's note** Springer Nature remains neutral with regard to jurisdictional claims in published maps and institutional affiliations.



**Open Access** This article is licensed under a Creative Commons Attribution 4.0 International License, which permits use, sharing, adaptation, distribution and reproduction in any medium or format, as long as you give appropriate credit to the original author(s) and the source, provide a link to the Creative Commons license, and indicate if changes were made. The images or other third party material in this article are included in the article's Creative Commons license, unless indicated otherwise in a credit line to the material. If material is not included in the article's Creative Commons license and your intended use is not permitted by statutory regulation or exceeds the permitted use, you will need to obtain permission directly from the copyright holder. To view a copy of this license, visit <http://creativecommons.org/licenses/by/4.0/>.

© The Author(s) 2023